Låstad, J., and J. Safarian. 2026. Vacuum refining techniques for End-of-life solar silicon. In *Silicon for the chemical and solar industry XVIII,* edited by M. Tangstad, H. Rong, A. Valderhaug, B. Andresen, H. Dalaker, and I. G. Page. Kristiansand, Norway, September 7–10, 2026. https://doi.org/10.55669/oa900804

Vacuum refining techniques for End-of-life solar silicon

J. Låstad[1], J. Safarian[2]
[1]NTNU, Norway, Jonas.Lastad@ntnu.no
[2]NTNU, Norway, Jafar.Safarian@ntnu.no

Keywords: Photovoltaics, Silicon, Vacuum refining, low vacuum gas flow

Abstract – End-of-life (EoL) photovoltaic (PV) silicon wafers are currently downcycled into lower value metallurgical silicon, losing much of its value. To address this, EoL silicon purification via vacuum refining was studied using the temperatures 1450 °C, 1600 °C, 1700 °C and a pressure of approximately 20 Pa. The sample vapor was collected by a novel approach utilizing a water-cooled plate condenser placed above the crucible holding molten silicon. The condensate and refined silicon samples were studied using glow discharge mass spectroscopy (GDMS). The results indicated that the condensation technique provided improved mass flux data. The impact of temperature indicated improved silicon yield with increased temperature. It was found that the evaporation from the melt, and hence the corresponding deposition on the condenser surface are affected by temperature and it is the highest at 1700C°, and the lowest at 1600C°. This could be explained by a surface slag layer originating from glass component and passivated layers impacted the mass transfer rate during vacuum refining by limiting the effective area of the melt due to partially surface coverage. This impact was reduced at 1700 °C temperature, where deoxidation of the melt and slag phase removal occurred. Regarding the properties of the material, a mechanism for mass transport of elements under vacuum for processing EoL PV silicon was proposed.

1. INTRODUCTION

Waste from the spent solar panels is a growing issue and current estimates reach 78 million tons of PV waste by 2050. Processes are being developed for recycling the bulk of the panel, namely glass and aluminum, as well as for the valuable silver electric busbars (Wade et al., 2016). However, the remaining wafer, which retains the value of higher purity, tends to be downcycled into metallurgical grade silicon. This results in the potential cost of upgrading the spent PV silicon by the existing Siemens process, which is both costly and has a high impact on climate.(Chen et al., 2023) Estimates for energy consumption for upgrading metallurgical Si to solar grade (SoG) polysilicon reaches 63.9 kWh per kg Si compared with only 12 kWh/kg for the initial smelting of metallurgical grade Si (Frischknecht et al., 2015). This estimate informs the headroom of alternative processes for reducing energy consumption.

Vacuum refining is a potential approach suited for recycling EoL PV silicon as the technique exploits the low volatility of silicon compared with most other metals.(Harris and Davenport, 1982) The technique is also suited for achieving high purity silicon as the purification is not dependent on an equilibrium, meaning that the concentration of volatile elements approaches zero. (Safarian and Tangstad, 2012b)However, all the mechanisms of mass transfer are not completely understood for all the relevant vacuum refining conditions. At low to medium vacuum the impact of chemical reactions in the gas phase are poorly understood, but has been found to modify the mass transfer through the gas phase.(Hoseinpur et al., 2021)

Studying the degree of purification during vacuum refining of high purity substances such as for solar grade silicon poses a challenge as the difference in purity between the treated and untreated samples are minimal as the concentrations are low already. The concentrations also approach in the order of 0.1PPM which is the detection limit for certain analytical techniques introducing uncertainty (Di Sabatino, 2014). This paper aims to explore medium vacuum conditions for upgrading the purity of EoL PV silicon using a novel sample collection technique, with the goal of obtaining solar grade feedstock quality.

2. THEORY

2.1 End-of-Lifeo photovoltaic material characteristics

EoL PV waste consists of a mix of panel designs; old panel types consisted of primarily P type panels where the emitter layer is doped with phosphorous and the bulk doped with boron. Tunnel Oxide Passivated Contact (TOPCon) cell structure as presented in Figure 1 is the leading PV cell in 2026. The figure represents the different layers such as of the TOPCon cell. The dopant in the emitter and bulk layer depends on the wafer type and has historically been primarily P-type wafers with B in the bulk layer and P in the emitter. Newer cell designs using N-type wafers doped with P in the bulk and B in the emitter. The list of expected elements in the different layers of a PV Cell is presented in Table I. During recycling, the panel is typically disassembled and metal contacts recovered, leaving behind primarily the doped silicon wafer, but with contamination from glass and oxide wafer layers. (Vodapally and Ali, 2022)

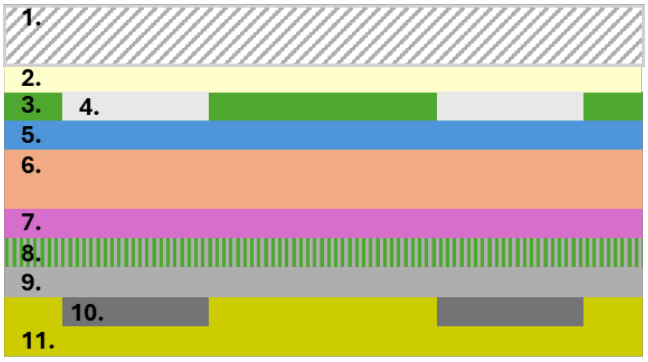

Figure 1 Schematic showing structure of a typical TOPCon panel. 1. PV glass, 2. Binding polymer, 3. Anti-reflective coating, 4. Front electrical contacts, 5. Doped emitter, 6. Bulk layer, 7. Doped Thin Film, 8. Tunnel oxide passivated rear contact, 9. Rear metallization, 10. Rear electrical contacts, and 11. Polymer backsheet.

Table I Element distribution in Si PV (Granata et al., 2014; Sharma, 2019; Lozac'h, Nunomura and Matsubara, 2020; Ghosh et al., 2022)

Layer	Element
Glass	MgO, Al_2O_3, SiO_2, CaO, TiO_2, SnO, K_2O, Sb_2O_3
Polymer	H, C, O
Anti reflective coating	MgF_2, Al_2O_3, $AlSiO_2$ SiN_x, TiO_2
Front contacts	Ni, Cu, Ag, Zn, Pb
Emitter layer	Si, B, Al, Ga
Bulk layer	Si, P, As
Back surface field	Si, P, As
Tunnel oxide layer	Si, Al, Ti, O
Rear metallization	Al, Ti, Ag
Rear electrical contact	Al, Zn, Sn, Pb
Polymer backsheet	H, C, O

Other elements may enter the waste stream due to poor sorting. Thin film PV panels such as CdTe panels pose a challenge as they introduce heavy metals such as cadmium or telluride. Furthermore, perovskite and tandem modules may introduce elements otherwise unaccounted for. However, these technologies are not dominant and, assuming adequate sorting, these potential contaminants are not considered (Sundaram, Benson and Mallick, 2016).

2.2 Vacuum refining

In vacuum refining, similarly to distillation, the differences in volatility between the components of a mixture are exploited to achieve a difference in mass transport rate and obtain a targeted composition. The technique utilizes the deviation equilibrium in pressure as the mass transport from the vapor source, or the melt, which approaches p_i^e and the vapor pressure on the cold surface which approaches $p_i^c \rightarrow 0$, here i denotes element i. This is calculated in equation [1] using standard vapor pressure p_i^0 of the elements and chemical activities a_i in the melt, activity coefficient γ_i and the molar concentration X_i. The activity coefficients can be assumed constant in dilute solution known as the Henrian activity coefficients γ_i^0, which is a valid assumption for all the minor elements, and can be assumed to be 1 for the silicon solvent. Metals with low volatility such as tungsten, iron, and silicon are well suited for this purification technique as they have low vapor pressures compared to most other elements. Silicon is particularly suited for vacuum refining as it has very low vapor pressure compared to most metals, as seen in Figure 2.

$$a_i = \frac{p_i^e}{p_i^0} = \gamma_i X_i \quad [1]$$

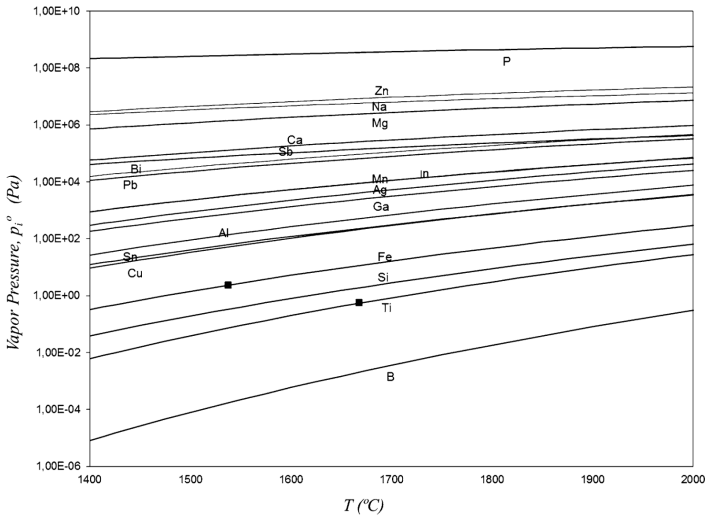

Figure 2 Vapor pressure of elements as a function of temperature, as calculated by (Safarian and Tangstad, 2012b).

The evaporation rate is controlled by the rate of transport through the different steps between the molten metal and the condensing surface. The steps are diffusion through the melt surface m, evaporation at melt-gas interface c, diffusion through the gas g and deposition d. Assuming no accumulation and that the system is in steady state, the coupled model can be presented as equation [2]. Where the mass flux for element i, $\dot{m}_i$ $\left[\frac{kg}{s}\right]$, is the momentary rate at the changing concentration c_i $[g/g\ Si]$ can be described following equation [3] using the mass transfer coefficient k_i $\left[\frac{m}{s}\right]$ in a 1st order reaction and area A assuming no interaction with the wall. For a first order reaction, the rate constant can be calculated using equation [4] (Safarian and Tangstad, 2012a) using the starting C_i and final C_c concentration of the metal, as well as the area A, volume V , and refining time t.

$$\dot{m}_i = \dot{m}_{m,i} = \dot{m}_{c,i} = \dot{m}_{g,i} = \dot{m}_{d,i} = \frac{dm}{dt} \quad [2]$$

$$\dot{m}_i = k_i * C_i * \rho_{Si} * A \quad [3]$$

$$k_i = \ln\left(\frac{C_s}{C_f}\right)\Big/\frac{A}{V}t \quad [4]$$

The total mass transport coefficient k_i can be calculated by taking the resistive sum of the different mass transport steps shown in equation [5]. These steps are mass transfer through melt boundary layer: $k_{m,i}$, mass transfer through evaporation $k_{c,i}$, mass transfer through gas phase $k_{g,i}$, and the condensation referenced as $k_{d,i}$, d representing deposition.

$$k_i = \left(\frac{1}{k_{m,i}} + \frac{1}{k_{c,i}} + \frac{1}{k_{g,i}} + \frac{1}{k_{d,i}}\right)^{-1} \quad [5]$$

Induction heating causes stirring in conductive melts, inducing a high surface velocity v_m, causing k_m to be large. Hoseinpur describes diffusion through the melt boundary layer as having a negligible impact on the flux under the relevant conditions and can be disregarded (Hoseinpur et al., 2021). The deposition rate has also been described as negligible (Malhotra, Mahajan and Sampath, 2006), leaving the evaporation rate and the gas transfer rate as the rate determining steps.

3. METHODS

The furnace used in this work, as presented in Figure 3, consists of the following parts:
The condensing plate for the collection of metal vapor is original and will be used for measuring the relative flux of the refining process. The dimensions of inner crucible were 96 mm high and 51 mm inner diameter. The distance between the bottom of the inner crucible and the cold plate was 130 mm. The thermocouple is positioned on the outside of the inner crucible and the space between the crucibles is packed with insulation. The placement of the thermocouple simplifies the geometry of the crucible, limiting the impact on gas flow. The insulation improves the accuracy of the thermocouple and holds crucible in place for sampling. The temperature T_b obtained from this thermocouple is approximate of the actual bulk temperature. From experience, the deviation is less than 50 °C from the actual value.

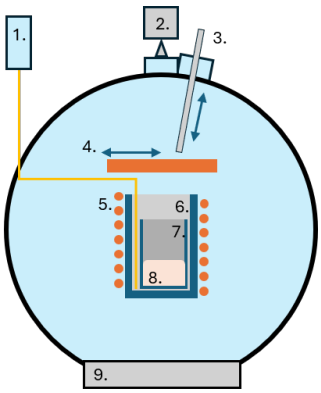

Figure 3 Schematic of vacuum induction furnace. 1. Thermocouple and 2. Pyrometer for measuring bulk temperature T_b and surface temperature T_s, 3. Quartz sampling tube for sampling the molten silicon without opening the furnace, 4. Vapor condenser for collecting the evaporated material, 5. Induction coil, 6. Outer graphite crucible, 7. Inner graphite crucible, 8. Molten Si sample, 9. Vacuum pump system.

A 100 g sample of mixed crushed EoL PV silicon with composition as presented in Figure 9 which had been separated, and treated for metal recovery was delivered by Fraunhofer CSP and used in each experiment, as seen in Figure 4, with a density 2.52 g/cm^3 (Mukai and Yuan, 2000) this corresponds to 39 682 mm^3 of molten Si, resulting a depth of 19.4 mm in the inner crucible.

Figure 4 Image of crucible setup and silicon sample.

Prior to the experiments, the crucibles are heated to remove volatile elements from the crucible and minimize contamination. Three vacuum refining experiments were performed, one each at surface temperatures T_s = 1450 °C, 1600 °C and 1700 °C. The holding time at the conditions was 60 minutes as indicated by the red lines, beginning when the vacuum reached 20 Pa. The measured temperatures are presented in Figure 5 – 7. With manual temperature controls, the temperature varied as seen in Figure 7 the sudden drop in bulk temperature T_b was caused by the shifting of the thermocouple, loosing contact with the inner crucible. The noise in the surface temperature data is caused by the condenser plate being moved in front of the pyrometer. Limited pumping rate and minimum pressure led to the pump being left running during the experiment, working at its highest rate, resulting in the presented pressure profiles rather than a set pressure, this is not believed to have a significant impact on the flux, as the change is small, and the curve is consistent between the experiments.

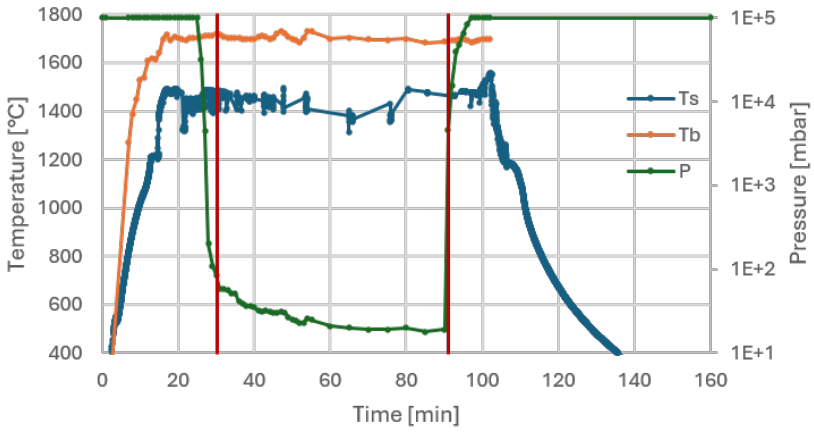

Figure 5 Furnace conditions [Ts=1450 °C].

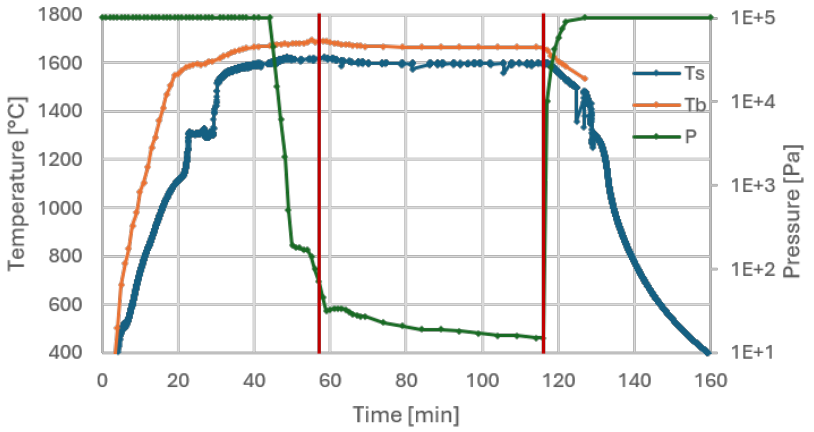

Figure 6 Furnace conditions [Ts=1600 °C].

Silicon samples were taken from the molten silicon by a pure quartz tube sampler that molten silicon was sucked into it. Once the melt reached the target temperature, once before making vacuum sampling was carried out, and again after re-pressurization after 60 minutes of refining. The samples were analyzed providing before and after compositions for the refining experiments. The vapor was deposited and collected on the water-cooled condenser plate as shown in Figure 3. The condenser plate obstructed the visibility of the pyrometer and hence was regularly moved aside for surface temperature measurements. This reduced the condensate collected for some seconds. However, the deposit loss is assumed to be insignificant in the total time of the refining. Collected metal and condensate samples were analyzed using Glow Discharge Mass Spectrometry (GDMS).

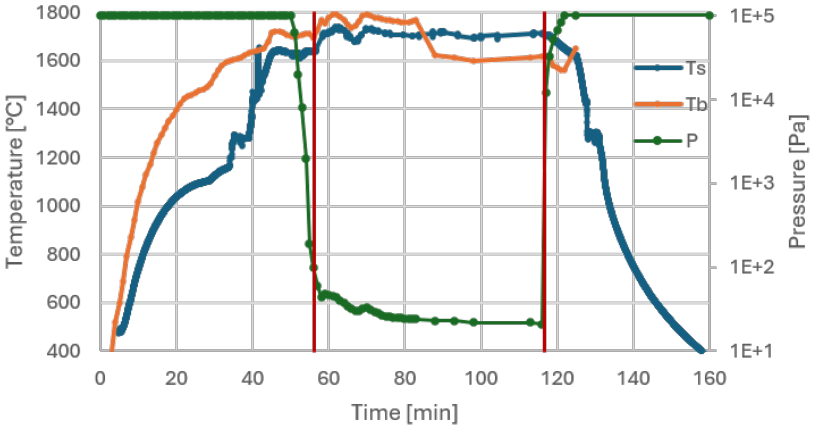

Figure 7 Furnace conditions [Ts=1700 °C].

4. RESULTS

4.1 Observations

As presented in Figure 5 and 6, the surface temperature T_s for the 1450 °C and 1600 °C experiments are consistently lower than the bulk. For the experiment at 1700 °C, shown in Figure 7, there is a sudden drop in bulk temperature T_b. This drop is suspected of being caused by displacement of the thermocouple, causing it to lose thermal contact with the melt or damage. The slightly lower surface temperature than the bulk is expected as the evaporation of silicon and other elements are endothermic and occurring at the surface of the melt. Once the target temperature had been reached and the vacuum chamber evacuated, a distinct vapor plume could be observed between the molten silicon surface and the condenser plate, as shown in Figure 8a. There is no visible plume bypassing the plate, indicating good vapor collection. The condensate could later be seen accumulating with dendrites on the plate as shown in Figure 8b. The change in mass for the crucible was minimal.

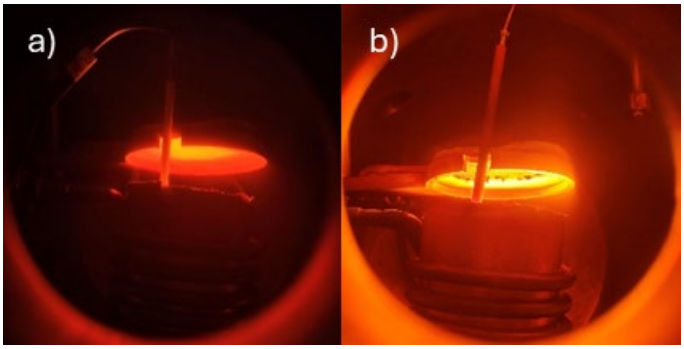

Figure 8 Images of crucible, induction coil, thermocouple, and condenser plate. A) Vapor cone visible shortly after reducing pressure. B) Dark patches of condensate visible on condenser plate.

4.2 Chemical analysis

GDMS analysis of silicon samples before and after refining is presented in Figure 9 and Figure 10 and shows minimal standard deviation in the analysis. There is significant spread in composition between the samples, despite being the same sample material. The concentration of impurities like B, Al, P, Ca, and Cu can be seen to increase after refining, loss of silicon could explain the non-volatile elements, but the volatiles indicate contamination. Carbon was detected in the metal but is assumed to have dissolved from the graphite crucible in the melt. There are differences in the concentrations of the samples, after melting. The batch refined at 1600 °C has higher concentrations of Na, K, Ca than the other temperatures. This is seen in both the before and after refining samples.

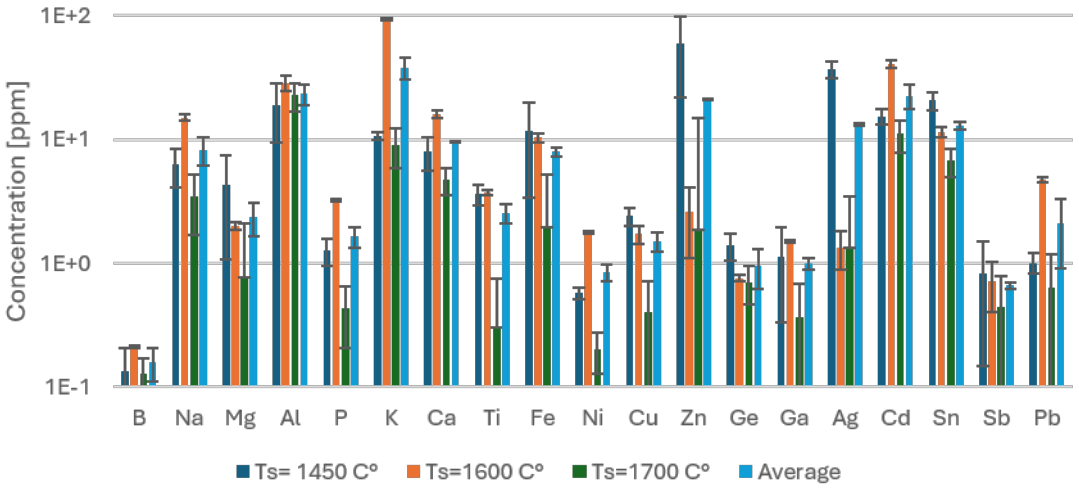

Figure 9 Starting compositions of molten silicon from GDMS analysis, individual samples and average. Error bars indicate standard deviation from analysis.

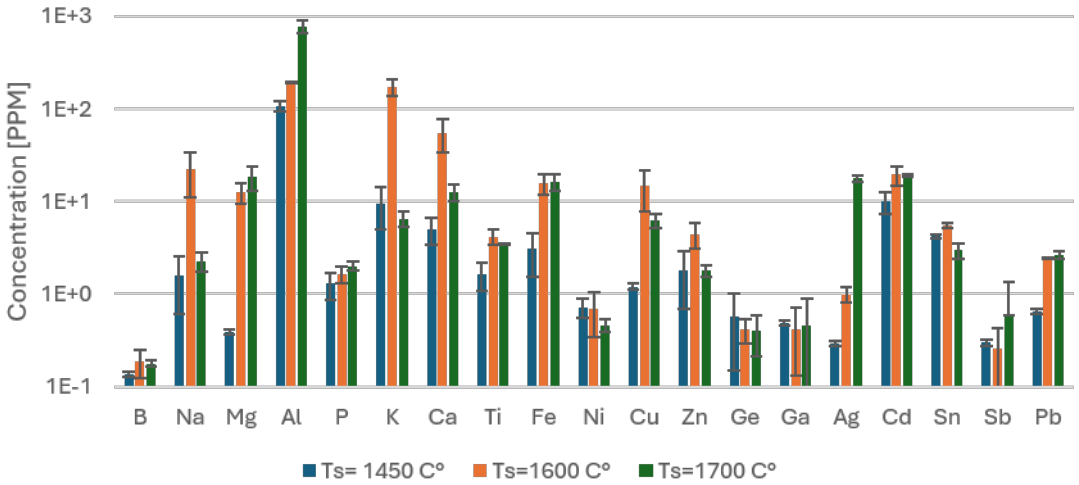

Figure 10 Final compositions of silicon melts measured by GDMS analysis, error bars indicate standard deviation.

The condensate formed during the experiments was collected and their masses are presented in Table II. These values can be used to calculate the mass flux. The 1600 °C sample deviates from the expected trend of increasing mass as temperature increases. The sample mass 1600 °C is significantly lighter than both the 1450 °C and 1700 °C samples, indicating less vapor in contact with the condenser for this experiment.

Table II Mass of collected condensate.

Sample	Mass [g]
Ts = 1450 °C	0.175
Ts = 1600 °C	0.096
Ts = 1700 °C	0.230

The condensate compositions are presented in Figure 11. The concentration of the impurities are higher orders of magnitude in the condensate than in the metal, with the exemption of Ti. This indicates they are removed from the metal faster than silicon, and Ti evaporation is insignificant as expected regarding its low vapor pressure (Fig. 1). The ratios between silicon and the different elements informs the relative flux α independent of the mass of the collected condensate. Higher temperatures correspond to lower silicon concentrations, indicating higher selectivity, mostly dominated by the increase in aluminum concentration. In a non-equilibrium reaction, a higher selectivity results in higher purity and silicon yield. K concentration is below the detectable limit for GDMS analysis despite the high concentration in the melt, and high volatility. The condensate also contained a detectable concentration of Ge, Ga and Cd which was absent from the analyses of the silicon metal. The presence of C in the condensate can be explained by the decomposition of the organic binder in the graphite or thermal insulator.

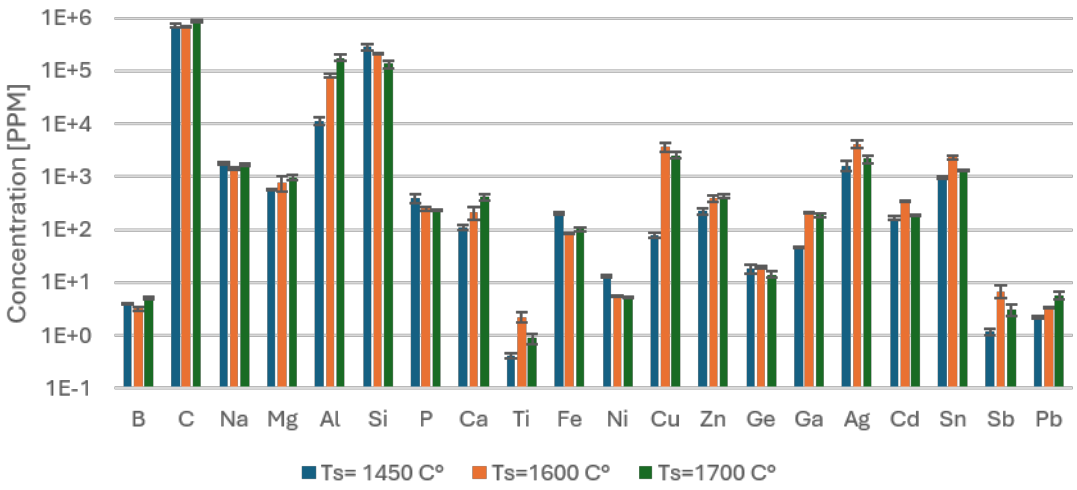

Figure 11 Composition of condensate by GDMS analysis.

5. DISCUSSION

5.1 Evaluating analysis

It is apparent that the measured initial concentrations of the samples varied. This may be explained by the presence of contaminants or from inhomogeneity in the samples. Figure 9 indicates that the inhomogeneity of the sample is a significant issue and sample melted at 1450°C contains more of some metallic impurities (Fe, Cu, Zn, Ag, Sn), while the sample melted at 1600°C contains more of the elements that are often in glass (Na, Al, K, Ti). The impact of this is exasperated by the low concentration, approaching the detectable limit of GDMS. As the concentrations are at ppm levels, the concentration of the melt is affected by even a small particle of the glass or a particle that has more metallic components. Hence, it is important to consider the initial composition of the melts for further calculations rather than the average composition presented in Figure 9. The condensate concentrations are multiple orders of magnitude greater than the corresponding metal samples and are useful for calculating mass flow.

The challenge for using the condensate is the sample collected quantity. When combining pyrometry and collection, time spent measuring temperature should therefore be subtracted from holding time. Furthermore, as can be seen in Figure 8b, there is a chance condensate could flake off and fall back into the crucible. This could potentially have caused the low mass of the condensate of the 1600 °C experiment and could explain the outlier concentration of Na, K, and Cu in this sample. However, no particles were found on the surface of the solidified sample, and this may or may not have occurred.

Considering experimental design, the flat condensing surface could have caused scattering of high volatility elements such as K, P, Zn and Pb. By texturing the surface, scattered particles would collide with the condenser multiple times before escaping to the furnace chamber. In theory of vacuum metallurgy, it is usually assumed that the atoms colliding with the cold surfaces are getting deposited due to losing the kinetic energy. However, the outer surface of the deposited layer may have high temperature and so these elements are scattered due to still high vapor pressure and kinetic energy. Texturing of the condenser surface would also double the effective surface area, improving adhesion thereby reducing the risk of scaling. Similarly, increasing the distance from the crucible opening, and size of the condenser, the area would reduce the heat flux, minimizing the vapor loss to the chamber.

There is a possibility of the vapor bypassing the condenser plate, however, the distribution of condensate on the cold plate shows a strong concentration towards the center (directly above the melt surface) and the gap between the crucible and condenser is small making this impact negligible. A larger concern is surface effects from the crucible, as the temperature of the crucible wall in upper position is lower than the molten silicon, and insignificant condensation was observed on the crucible top.

5.2 Mechanism of mass transfer in the system

The apparent mass flow of impurities into both the metal and condensate such as for aluminum, is improbable and challenges the calculation of mass transfer coefficients. A possible explanation of this is the presence of a slag phase, possibly formed from the small glass fragments, below micrometer size and the passivated layers of the wafer. This slag is a silicate phase that usually contains Na, Mg, Ca, Al, K, Ti, and some trace elements. Oxides from glass residue and passive layers such as SiO_2 and Al_2O_3 could contain the impurities detected. Given the composition and distribution as presented in Table I and incomplete separation during sorting, this is reasonable. The samples that were analyzed were taken from the bottom of the molten metal, where the suction of the melt to the quartz tube sampler was done. Therefore, the presence of a floating slag layer on top of the silicon melt would not be represented in the samples analyzed.

A thin slag layer would impact the flux in a non-linear way, as the slag layer consists of lower volatility oxides and may form a capping layer on the molten silicon as seen in Figure 12. Initially at low temperature of 1450 °C, the slag is semi-solid and clumps along the edges of the crucible. At higher temperature such as 1600 °C the slag thins and covers more of the silicon, reducing its effective surface area and therefore preventing the evaporation of the species from the melt surface. Figure 9 shows that the silicon for the test at 1600 °C has more elements that the slag contains (Na, K, Ca, and Al) than the test at 1450 °C. This indicates that we may have more slag for the test at 1600 °C and hence more Na, K, Ca and Al were transported to the silicon melt. Hence, less evaporation occurred for the test at 1600 °C, and it yielded less deposit mass on the condenser surface.

For the test at 1700 °C, there were lower concentrations of Na, Al, Ca, K than in the metal tested at 1600 °C as seen in Figure 9, and this may indicate less glass contamination and associated slag phase before the vacuum refining. However, for 1700 °C, the largest mass of the deposit on the condenser was observed. This means more evaporation in comparison with the test at 1600 °C. As for 1700 °C, the slag is more reactive with the silicon melt and causes deoxidation of the molten system (slag + metal) through the formation of SiO gas in the system. Hence, we may conclude that at higher temperatures, the silicon oxide is reduced forming SiO and CO gas, thereby slag is removed and so we have the increase of the evaporating area for the elements. This may cause a higher condensate mass for the test at 1700 °C, while the concentration of the components is not different from the other temperatures (Figure 11).

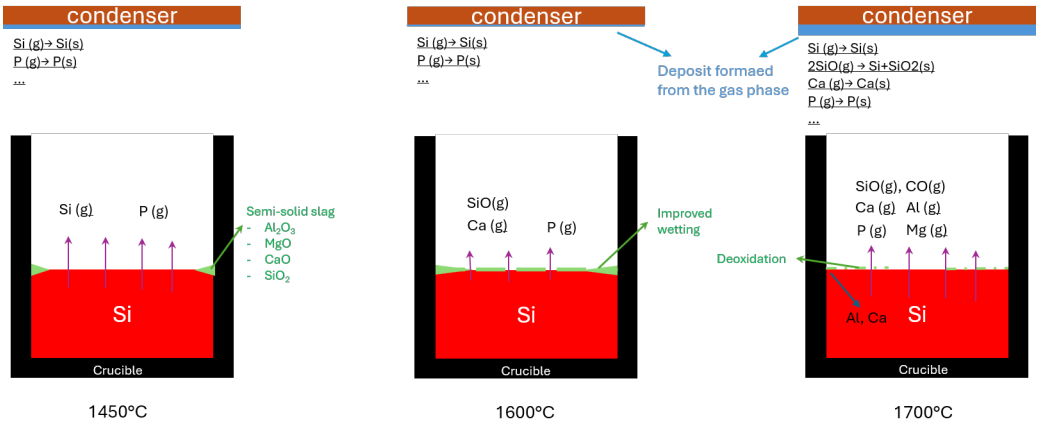

Figure 12 Schematic of the impact of a slag layer on the rate of evaporation as a function of temperature, and some typical condensation reactions from the vapor.

This mechanism is supported by thermodynamic calculations using HSC chemistry 10 (Metso, 2020) as seen in Figure 13 using a reference composition of 1mol Si, 1 mol C, and 0.1 mol of the slag components. The system changes around 1710 °C as deoxidation occurs as described by equations [6] to [9], forming SiO and CO. There is an equilibrium of metal and slag below the deoxidizing temperature, but with no oxide evaporation. The values can be considered representative of the activities and thereby evaporation rate.

$$SiO_2(l) + Si(l) = 2SiO(g) \quad [6]$$
$$SiO_2(l) + C(s) = SiO\ (g) + CO\ (g) \quad [7]$$
$$3Si(l) + Al_2O_3(s) = 3SiO\ (g) + 2Al(l) \quad [8]$$
$$Al_2O_3(s) + 3C(s) = 2Al + 3CO\ (g) \quad [9]$$

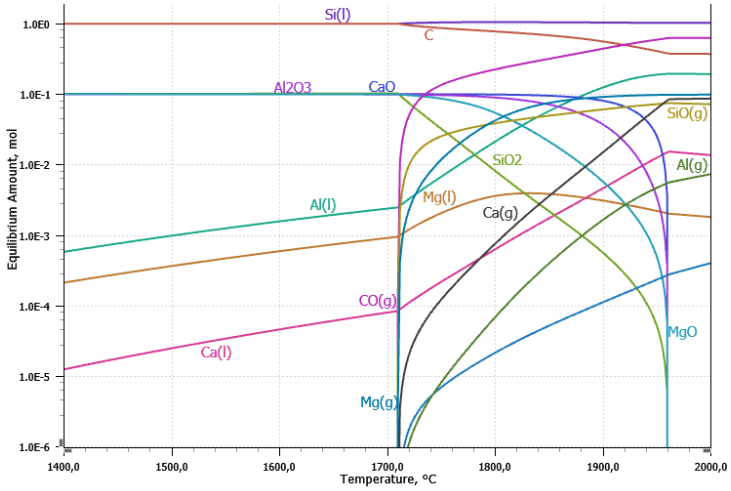

Figure 13 Equilibrium diagram of simulated Silicon-Slag system, calculated using HSC Chemistry.

5.3 Mass transport

The purity of the final product can be described by the measured concentrations of the treated sample as seen in Figure 10 or by applying the mass transfer regarding the condensate mass and composition. Considering the deoxidation reactions, slag elements simultaneous transport from slag to metal and evaporation from the metal would impact the evaporation rate calculated using the metal composition changes. This would also change the reaction order, as the concentration change is not only dependent on the evaporation rate. Figure 14 presents the composition of the melt as calculated by subtracting the mass of the elements in the condensate from the mass of the elements in the initial metal. Al and Cu reached negative, near zero values indicating more than complete removal or that those elements may originate from the slag. Cu might be explained by contamination from the copper plate while Al might be explained by the underrepresentation in the initial composition due to the slag layer or alumina in the feed silicon components seen in Table I. The change in elements such as B, Ti, Fe, and Ni is minimal as expected for the elements as they have low volatility compared with Si. Na, Mg, P, and Ga seem to drop at 1700 °C as expected from slag elements due to the slag reduction and the evaporation of the elements under vacuum. Compared with the samples from the melt, it indicates that K is still removed while not condensation on the condenser. The flux of the elements is high enough to significantly impact the purity of the sample positively, even in the given conditions.

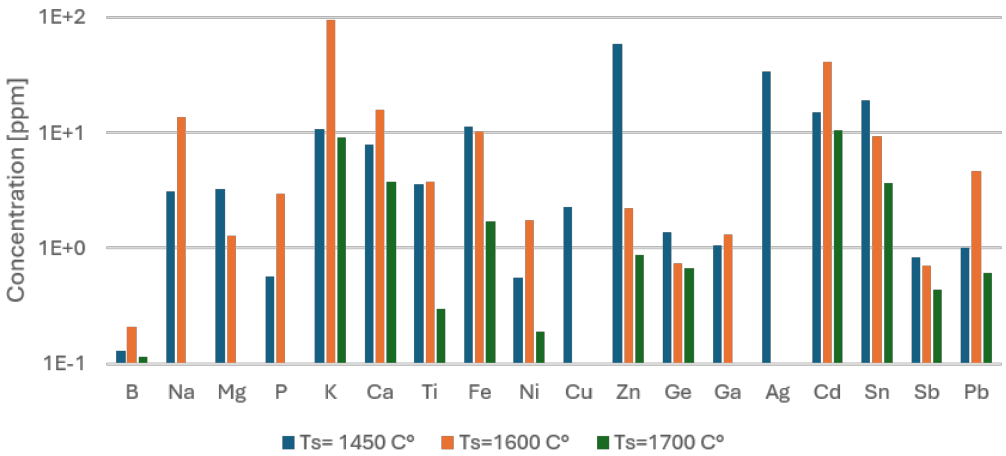

Figure 14 Calculated final composition of silicon using starting composition and mass transfer from condensate data, absent bars indicate negative values.

Assuming the collected condensate samples are representative, and a minimum of vapor was lost before collection, despite the unexpectedly low condensate mass from the 1600 °C experiment, the approximate mass transport coefficients can be calculated following equation [4]. The final composition of the metal is first calculated using the mass of the condensate, subsequently multiplying the concentration of the element with the mass of the condensate, dividing by time, thereby obtaining the mass flux of the element.

The flux can then be divided by initial concentration, area and density. The resulting mass transfer coefficients are presented in Figure 15. There is a correlation between increasing temperature and mass transfer. The values for the elements B and Ni, and Pb are higher than expected, being higher than silicon despite their vapor pressures being lower than silicon. Comparing the experimental mass transfer coefficients with theoretical ones is difficult as medium pressure regimes as this study are not well modelled. The usefulness of these conditions for vacuum refining is questionable as the impact of the process is limited. Deeper understanding of these medium vacuum environments as described by (Hoseinpur et al., 2021) is needed to improve selectivity. It is worth to note that in literature, most studies are on silicon samples without slag (glass) and the existence of small amount of glass in the feed is affecting the chemistry of the system and the surface of the melt.

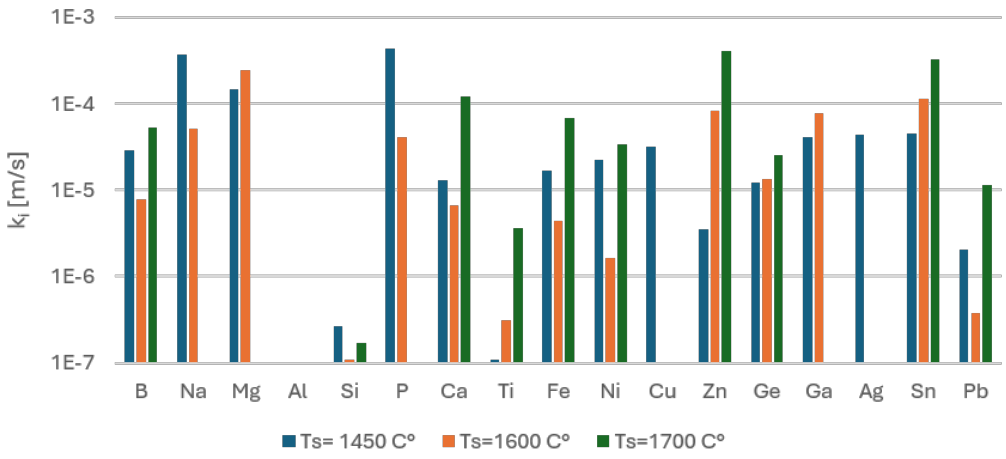

Figure 15 The overall mass transfer coefficients k_i calculated from mass and composition of condensate. Absent values indicate infinite, due to excess concentration in the condensate.

The mass transfer coefficient can also be calculated from the change in concentration in the metal for the purpose of corroboration. It is assumed that there is no change in silicon mass, which is appropriate as the relative mass change is minimal. The resulting plot in Figure 16 is sparse, indicating negative values reflecting an increase in concentration. Though being sparse indicating, disregarding the negative values, that the approximate magnitude is similar for most elements. Aluminum consistently increased in concentration as it is expected to have higher mass transport of Al (from slag or other components of EoL Si) to the silicon melt than its evaporation under vacuum. When comparing the mass transfer coefficient between the condensate and metal, the lower values for known volatiles such as K, Ca, Zn, and Pb in the condensate might indicate scattering caused by inadequate gas cooling performance. These elements have lower condensation temperatures and higher vapor pressures, and hence more chance to leave a condensate over the furnace chamber or reach the vacuum pump.

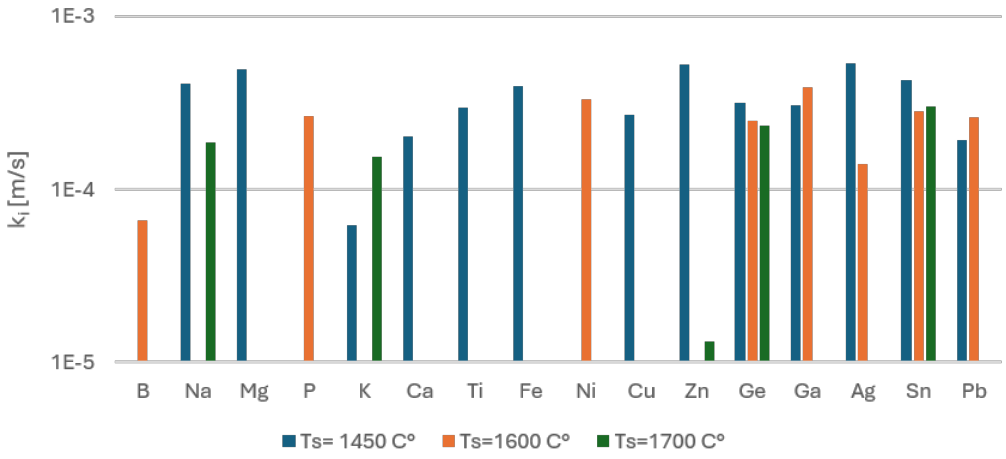

Figure 16 Mass transfer coefficients k_i calculated from the change in metal composition. Absent values indicate negative mass transfer.

6. CONCLUSION

This study demonstrates that vacuum refining is a viable technique for purification and recycling EoL PV silicon waste, evaporating volatile dopants and metallic impurities. Exploiting the differences in vapor pressures, the technique is still useful for already pure samples.

- Most of the impurities in the EoL PV Si particles are removed via the vacuum induction refining process at elevated temperatures.
- The mass transfer coefficients calculated for the experiments were higher than the theoretical values, probably due to complexity due to the existence of an adjacent thin molten slag phase.
- Mass transfer coefficients increase with increasing temperature, and lower values for many elements (B, Na, Si, P, Ca, Fe, Ni and Pb) at 1600 °C is attributed to silicon melt coverage with a molten slag.
- The applied novel method of vapor collection yields improved chemical resolution, with issues regarding complete sample collection.
- Increased temperature improved silicon yield and higher purity, and at 1700 °C it yielded the highest purification with insignificant silicon loss.
- Holding time at current conditions is insufficient for achieving high purity silicon, and longer time is needed to reach promising purity.
- Condensate samples provided more reliable data for mass transfer evaluation than the change in metal composition.
- A slag layer should be considered for the purpose of vacuum refining EoL PV Si as this can impact evaporation rate by limiting the effective area of the evaporating metal. The removal of glass particles prior to vacuum refining is crucial.

7. ACKNOWLEDGEMENTS

The authors gratefully acknowledge the financial support from the European Union to Apollo EU project in Horizon Europe program under the grant number of 101122277.

8. REFERENCES

Chen, P.-H., Chen, W.-S., Lee, C.-H., Wu, J.-Y., Chen, P.-H., Chen, W.-S., Lee, C.-H. and Wu, J.-Y., 2023. Comprehensive Review of Crystalline Silicon Solar Panel Recycling: From Historical Context to Advanced Techniques. *Sustainability*, [online] 16(1). https://doi.org/10.3390/su16010060.

Di Sabatino, M., 2014. Detection limits for glow discharge mass spectrometry (GDMS) analyses of impurities in solar cell silicon. *Measurement*, 50, pp.135–140. https://doi.org/10.1016/j.measurement.2013.12.024.

Frischknecht, R., Itten, R., Sinha, P., De Wild-Scholten, M., Zhang, J., Heath, G. and Olson, C., 2015. *Life Cycle Inventories and Life Cycle Assessments of Photovoltaic Systems*. [online] p.NREL/TP--6A20-73853, IEA-PVPS-TASK-12, IEA-PVPS-12-04:2015. https://doi.org/10.2172/1561526.

Ghosh, D.K., Bose, S., Das, G., Acharyya, S., Nandi, A., Mukhopadhyay, S. and Sengupta, A., 2022. Fundamentals, present status and future perspective of TOPCon solar cells: A comprehensive review. *Surfaces and Interfaces*, 30, p.101917. https://doi.org/10.1016/j.surfin.2022.101917.

Granata, G., Pagnanelli, F., Moscardini, E., Havlik, T. and Toro, L., 2014. Recycling of photovoltaic panels by physical operations. *Solar Energy Materials and Solar Cells*, 123, pp.239–248. https://doi.org/10.1016/j.solmat.2014.01.012.

Harris, R. and Davenport, W.G., 1982. Vacuum distillation of liquid metals: Part I. Theory and experimental study. *Metallurgical Transactions B*, 13(4), pp.581–588. https://doi.org/10.1007/BF02650015.

Hoseinpur, A., Andersson, S., Tang, K. and Safarian, J., 2021. Selective Vacuum Evaporation by the Control of the Chemistry of Gas Phase in Vacuum Refining of Si. *Langmuir*, 37(24), pp.7473–7485. https://doi.org/10.1021/acs.langmuir.1c00876.

Lozac'h, M., Nunomura, S. and Matsubara, K., 2020. Double-sided TOPCon solar cells on textured wafer with ALD SiOx layer. *Solar Energy Materials and Solar Cells*, 207, p.110357. https://doi.org/10.1016/j.solmat.2019.110357.

Malhotra, C.P., Mahajan, R.L. and Sampath, W.S., 2006. High Knudsen Number Physical Vapor Deposition: Predicting Deposition Rates and Uniformity. *Journal of Heat Transfer*, 129(11), pp.1546–1553. https://doi.org/10.1115/1.2712855.

Metso, 2020. *HSC Chemistry 10*. Available at: <https://www.metso.com/portfolio/hsc-chemistry/>.

Mukai, K. and Yuan, Z., 2000. Measurement of the Density of Molten Silicon by a Modified Sessile Drop Method. *Materials Transactions, JIM*, 41(2), pp.323–330. https://doi.org/10.2320/matertrans1989.41.323.

Safarian, J. and Tangstad, M., 2012a. Kinetics and Mechanism of Phosphorus Removal from Silicon in Vacuum Induction Refining. 31(1), pp.73–81. https://doi.org/10.1515/htmp.2011.143.

Safarian, J. and Tangstad, M., 2012b. Vacuum Refining of Molten Silicon. *Metallurgical and Materials Transactions B*, 43(6), pp.1427–1445. https://doi.org/10.1007/s11663-012-9728-1.

Sharma, R., 2019. Effect of obliquity of incident light on the performance of silicon solar cells. *Heliyon*, 5(7), p.e01965. https://doi.org/10.1016/j.heliyon.2019.e01965.

Sundaram, S., Benson, D. and Mallick, T.K., 2016. Chapter 2 - Overview of the PV Industry and Different Technologies. In: *Solar Photovoltaic Technology Production*. [online] Academic Press. pp.7–22. https://doi.org/10.1016/B978-0-12-802953-4.00002-0.

Vodapally, S.N. and Ali, M.H., 2022. A Comprehensive Review of Solar Photovoltaic (PV) Technologies, Architecture, and Its Applications to Improved Efficiency. *Energies*, [online] 16(1). https://doi.org/10.3390/en16010319.

Wade, A., Heath, G., Weckend, S., Wambach, K., Sinha, P., Jia, Z., Komoto, K. and Sander, K., 2016. *IRENA and IEA PVPS (2016) - End-of-Life Management: Solar Photovoltaic Panels*.

Jonas Låstad
PhD Candidate, NTNU

Jonas Låstad works as a part of the EU funded Apollo project researching techniques for recycling end of life PV silicon. Here he researches both hydrometallurgical and vacuum refining techniques of silicon. He completed his bachelor's degree in materials engineering at the Norwegian University of Science and technology with his work on hydrogen reduction of deep-sea manganese ore. He completed his master's degree at the same university with his work on production of electrolytic manganese dioxide from hydrogen reduced manganese ore.